Sound & Vibration 2026, 60(4), 4311.
doi: https://doi.org/10.59400/sv4311

Article

Optimal design of a high-temperature ultrasonic vibration device

Lanphuong Nguyen[1,*], **Chinghua Hung**[2]

[1] School of Mechanical Engineering, Hanoi University of Science and Technology, Hanoi 100000, Vietnam
[2] Department of Mechanical Engineering, National Yang Ming Chiao Tung University, Hsinchu City 300093, Taiwan
*** Corresponding author:** Lanphuong Nguyen, phuong.nguyenlan@hust.edu.vn

CITATION

Nguyen L, Hung C. Optimal design of a high-temperature ultrasonic vibration device. Sound & Vibration. 2026; 60(4): 4311. https://doi.org/10.59400/sv4311

ARTICLE INFO

Received: 27 April 2026
Revised: 18 May 2026
Accepted: 25 May 2026
Available online: 21 July 2026

Abstract: Ultrasonic vibration-assisted manufacturing has emerged as a transformative method for machining hard-to-machine advanced materials. However, implementing these systems in precision high-temperature manufacturing processes like hot glass embossing introduces significant technical challenges due to severe thermal frequency drift and a degradation in output displacement uniformity. This study addresses these issues by presenting a comprehensive multi-physics numerical optimization framework for a 35 kHz high-temperature ultrasonic vibration device. Utilizing a coupled-field Finite Element Analysis (FEA) methodology in ANSYS, the steady-state thermal profile and its corresponding thermo-structural impact on the system's resonant frequencies and vibration characteristics were accurately modeled and verified. Shape optimization was executed through an automated coupling loop between the FEA workspace and the advanced numerical optimization platform, SmartDO. The results demonstrate that the optimization scheme successfully established a refined horn geometry that accommodates thermal degradation effects. Experimental validation conducted at an operating temperature of 500 °C confirmed that the optimized design maintained structural deviations within a narrow, manageable resonance window (84–99 Hz) while significantly improving output surface displacement distribution. The finalized device achieved an exceptional experimental amplitude uniformity of 8.20%, which matches the numerical simulation trend closely.

Keywords: ultrasonic vibration device; high temperature; finite element analysis; optimal design; amplitude uniformity; resonance frequency

1. Introduction

Ultrasonic vibration-assisted manufacturing has emerged as a transformative paradigm in modern production, offering a sophisticated solution to the inherent limitations of conventional machining. By superimposing high-frequency mechanical oscillations—typically exceeding 20 kHz—onto traditional manufacturing tools, this technology facilitates the processing of "hard-to-machine" materials that were previously deemed economically or technically unviable. The fundamental mechanism of ultrasonic vibration-assisted manufacturing involves a synergistic combination of high-rate impact, reduced average friction, and altered material deformation kinematics.

In the contemporary industrial landscape, particularly within the 5G telecommunications and aerospace sectors, the demand for advanced materials such as Silicon Carbide (SiC) and Silicon Carbide particulate-reinforced Aluminum (SiCp/Al) composites has grown exponentially. For these applications, ultrasonic-assisted grinding (UAG) has become the gold standard for achieving superior surface integrity and reduced machining forces. Research indicates that high-frequency vibration suppresses brittle fracture modes and promotes a ductile-regime material removal process [1]. By optimizing the interaction between the abrasive grains and the workpiece, UAG achieves significantly higher material removal rates while simultaneously mitigating common industrial hurdles such as tool clogging and excessive diamond grit wear [2,3].

Beyond traditional subtractive machining, the utility of ultrasonic energy has recently expanded into the stabilization and refinement of microstructures in high-power joining and additive processes. In the field of Laser-Arc Hybrid Welding, studies conducted through 2025 have demonstrated that applying ultrasonic vibration (ranging from 60 W to 240 W) to the lower surface of the weld pool significantly alters weld morphology [4]. For ultra-high-strength steel (UHSS), this assistance facilitates a transition in the weld cross-section from a restrictive “goblet” shape to a more robust “inverted triangle” [5].

In the domain of additive manufacturing (AM), specifically Wire Arc Additive Manufacturing (WAAM), the integration of ultrasonic energy through 2026 has revolutionized grain refinement and mechanical performance. A novel approach utilizing meltable ultrasonic probes (MUPA-WAAM) allows for the direct delivery of acoustic energy into the molten pool. This technique leverages the cavitation effect to fracture dendrites and refine microstructures, effectively reducing the average grain size in Al-Mg alloys from 39 μm to 14 μm [6]. The resulting thermal and acoustic energy promotes faster melting, increasing deposition productivity by as much as 286.9% while simultaneously enhancing ultimate tensile and yield strengths.

As the global manufacturing landscape shifts toward precision processes like thermal nanoimprinting and hot glass embossing—driven by the demand for 5G optical components and advanced sensors—the stability of the ultrasonic system becomes paramount. Ultrasonic assistance facilitates these “hot” processes by reducing interface friction and enhancing material flow [7–9]. However, the high-temperature environment (up to 500 °C) introduces significant technical complexities.

The core of these systems, the transducer and horn assembly, must be precisely tuned to achieve resonance with the electronic signal generator. Nevertheless, elevated temperatures induce a “thermal drift” that degrades the piezoelectric properties of the transducers and shifts the system's resonant frequency. Yu et al. [10] investigated these thermal effects, noting that temperature rises—whether caused by external heat sources or internal dielectric loss—significantly alter the fracture toughness of piezoelectric materials. These thermal sensitivities remain a primary barrier to the widespread deployment of such systems in harsh industrial environments [11].

When optimizing ultrasonic devices for extreme high-temperature environments, the thermal boundary interfaces play an instrumental role in overall acoustic performance. Because thermal contact conductance (TCC) across structural joints is highly temperature-dependent and sensitive to contact pressure, accurate interface characterization is critical to prevent frequency drift. Recent literature offers foundational fractal modeling methodologies for analyzing these rough contact interfaces. For instance, Sun and Xing [12] developed a fractal TCC model based on elliptical asperities, demonstrating that contact load, fractal dimension, and asperity eccentricity positively correlate with TCC, whereas higher fractal roughness degrades interface conductance. To capture multi-scale mechanics, Zhao et al. [13] established a three-dimensional fractal theory model accounting for elastic, elastic-plastic, and plastic micro-deformations. Their findings revealed that while TCC is heavily driven by elastic-plastic asperity interactions, air-medium thermal conductance within microgaps cannot be ignored under low contact loads. Furthermore, Sun [14] expanded this framework by proposing a fractal TCC model that integrates macro-scale substrate deformation alongside the three standard asperity deformation modes. Their results indicated that for high fractal dimensions ($D > 2.5$), the rate of TCC increase accelerates rapidly with increasing contact load. Integrating these micro-surface heat transfer mechanisms provides the theoretical basis necessary to calculate precise localized thermal profiles across high-power ultrasonic structural assemblies.

Historically, industrial design for these vibration systems has relied on approximate analytical solutions and empirical formulas for initial fabrication. This approach is inherently inefficient, often requiring multiple “trial-and-error” iterations to reach the target frequency. When these systems operate at 500 °C, material properties such as the Young’s modulus of stainless steel and titanium components undergo non-linear shifts. These variations lead to a critical mismatch in resonant frequency and a degradation in the uniformity of vibration amplitude across the output face.

Achieving a uniform displacement distribution at the output end of an ultrasonic horn is the primary challenge in high-temperature design, as non-uniform vibration leads to uneven stress distribution and compromised product quality. To address this, researchers have turned to advanced numerical optimization. Afshari and Arezoo [15] utilized topology optimization to design wide ultrasonic horns, employing a two-objective procedure that achieved improvements in amplitude uniformity of up to 584.5%. In the realm of large-scale 3D modeling, Schmidt et al. [16] pioneered gradient-based shape optimization within 3D time-domain simulations. By utilizing the FEniCS framework to handle billions of unknowns, they optimized the transmission efficiency of wave-guiding devices, a method critical for high-power industrial horns. Further innovations by Dong et al. [17, 18] introduced efficient multimodal-based shape optimization. This methodology enables “subwavelength perfect transmission,” outperforming traditional discrete-model approaches in both narrowband and wideband applications. Additionally, the study of complex geometries, such as the hollow catenoidal horn profiles analyzed by Mubashir et al. [19], has highlighted how modal and harmonic analysis in ANSYS can effectively identify resonant characteristics and equivalent stresses in composite machining environments.

To solve the above issues, Addamo et al. [20] proposed a two-objective topology optimization algorithm using the evolutionary structural optimization (ESO) method to design wide ultrasonic horns that achieve uniform output vibration and specific resonance frequencies. Besides that, a level-set topology optimization method was utilized to design large ultrasonic bonding tools with uniform vibration distributions, minimizing fabrication errors in resonance frequency and flatness [21]. While Finite Element Analysis (FEA) has been widely adopted to simulate ultrasonic behavior, the complex coupling between thermal expansion and structural dynamics at elevated temperatures remains an underdeveloped area. Accurate prediction requires a multi-physics approach that considers how temperature gradients affect material parameters, which in turn dictate the system's resonant behavior.

To bridge these research gaps, this manuscript details an advanced multi-physics shape optimization framework designed to mitigate thermal drift and maintain acoustic stability. The core novelty and primary technical contributions of this study are itemized as follows:

- Thermal-acoustic coupling framework: Developed an automated structural optimization workflow that tightly couples continuous non-linear temperature gradients with structural modal dynamics.
- Empirical material integration: Integrated explicit temperature-dependent Young's modulus formulations for SUS304 components to capture accurate high-temperature acoustic profiles up to 500 °C.
- Uniformity enhancement under severe gradients: Achieved a reduction in output end-face displacement variations to below 7% through automated geometric parameter adjustment via SmartDO.
- Experimental verification: Conducted high-power experimental validation combining laser displacement monitoring and network frequency analysis to confirm simulation accuracy under real production loads.

The remainder of this manuscript is structured as follows: Section 2 details the components of the ultrasonic stack, governing mathematical equations, and the automated SmartDO-ANSYS integration workflow. Section 3 presents the optimization results for various output face configurations and details structural modal behaviors, and Section 4 summarizes key conclusions, study limitations, and prospective areas for future research.

2. Method

2.1. Theoretical principles

2.1.1. Components of an ultrasonic vibration device

Typically, an ultrasonic vibration device is composed of three primary elements: a piezoelectric transducer, a booster, and a horn. The process begins with a signal generator supplying an electrical input to the transducer, which subsequently converts it into mechanical oscillations.

Industrial transducers are typically categorized into two types: magnetostrictive transducers and piezoelectric transducers. Since piezoelectric transducers have become widely used in piezoelectric switches, printheads, and piezoelectric ceramic relays in recent years, this study used a piezoelectric transducer manufactured by Jinghua Ultrasonic Co., Ltd. This piezoelectric transducer is a stacked type, meaning it consists of multiple piezoelectric materials stacked together, as shown in **Figure 1**. The arrows on the piezoelectric elements in the figure indicate the polarization direction. When the potential difference between the upper and lower surfaces of the piezoelectric element aligns with the polarization direction, the piezoelectric material will exhibit positive displacement. When voltage is applied to the odd-numbered and even-numbered surfaces of the piezoelectric stack, and the polarization directions are both aligned, the displacement of the piezoelectric material will cancel each other out as one increases and the other decreases. If the polarization direction of the odd-numbered layers is opposite to that of the even-numbered layers, the displacement of the piezoelectric material will increase or decrease simultaneously.

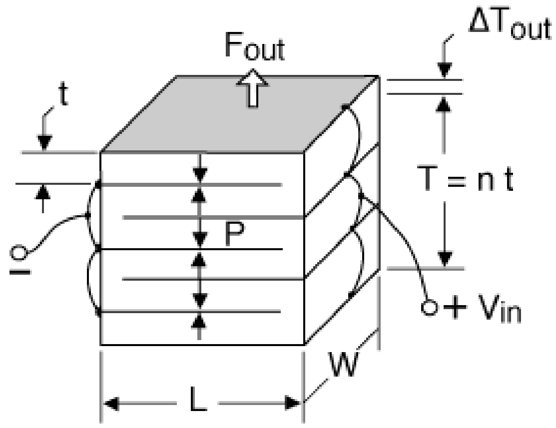

Figure 1. Schematic diagram of multilayer piezoelectric sheet structure [22].

The booster (also known as an amplitude transformer) serves as the intermediate bridge between the piezoelectric transducer and the horn. While the transducer generates the initial mechanical vibration through the piezoelectric effect, its output amplitude is often insufficient for industrial applications like welding or high-temperature glass embossing. The booster performs three critical functions within the acoustic stack: amplitude transformation (amplification or reduction), mounting node, and energy transmission and resonance matching. The booster ensures that the acoustic energy flows efficiently from the transducer to the horn. It must be precisely tuned to the same resonant frequency as the other components.

The horn is primarily used to adjust the energy density of the ultrasonic input to obtain the desired ultrasonic energy distribution, which has a decisive influence on the amplitude uniformity of the vibration system. Generally, horns come in four main shapes: step, conical, exponential, and catenoidal, with various combinations of these four types. The design goal is primarily to maximize amplitude amplification. However, its natural frequency must match the frequency of the electronic signal generator; otherwise, it will lead to changes in the characteristics and modes of the vibration system, affecting the transmission of ultrasonic vibration energy and causing phenomena such as resonant frequency shift, reduced amplitude amplification, the appearance of polarization and tortuosity modes, and uneven amplitude distribution. Therefore, the selection and design of the horn have a decisive impact on the vibration characteristics and performance of the entire vibration system. **Figure 2** shows various types of horns.

Figure 2. Horns of various geometries [23].

Common ultrasonic transmission modes include longitudinal waves, transverse waves, surface waves, torsional waves, and composite waves composed of two or more waveforms. The ultrasonic vibration system used in this study adopts the longitudinal wave mode, in which the direction of medium vibration is consistent with the direction of wave propagation, thus effectively utilizing the energy of ultrasonic waves. In isotropic solid materials, the wave velocity can be obtained by the following approximate theory [24]:

$$c_L = \sqrt{\frac{E}{\rho}} \tag{1}$$

where E and ρ are Young's modulus and density, respectively, and the wavelength is

$$\lambda = \frac{c_L}{f} = \frac{1}{f}\sqrt{\frac{E}{\rho}} \tag{2}$$

where f is the resonance frequency of an ultrasonic vibration device. In a longitudinal vibration mode, multiples of ($\lambda/2$) can be used as references for setting the device length. For an ultrasonic horn using longitudinal wave modes, its length must be half the longitudinal wavelength transmitted within the solid, or an integer multiple of half the wavelength. The theoretical length of the horn can be calculated from a given frequency and the ultrasonic longitudinal wavelength in the material using Equation (2); therefore, the horn length is related to the resonant frequency. However, these parameters change with variations in the horn's temperature distribution, making it more difficult to determine the horn length theoretically. Therefore, this study will combine experimental measurements and finite element analysis to explore the relationship between temperature and resonant frequency and will utilize an optimization method to design an ultrasonic vibration device.

2.1.2. Analysis of ultrasonic vibration devices

Most structural design methodologies aim to completely suppress structural vibrations to avoid cyclic fatigue failure. Traditional methodologies that rely solely on room-temperature mechanical properties fail to predict acoustic performance accurately under severe thermal loading because they do not account for localized shifts in acoustic velocity ($c_L = \sqrt{E/\rho}$) caused by sharp temperature gradients. However, this study applies ultrasonic vibration to the manufacturing process, so the system's resonant frequency must match the frequency of the electronic signal generator to achieve resonance. **Figure 3** shows the necessary analysis of an ultrasonic vibration device.

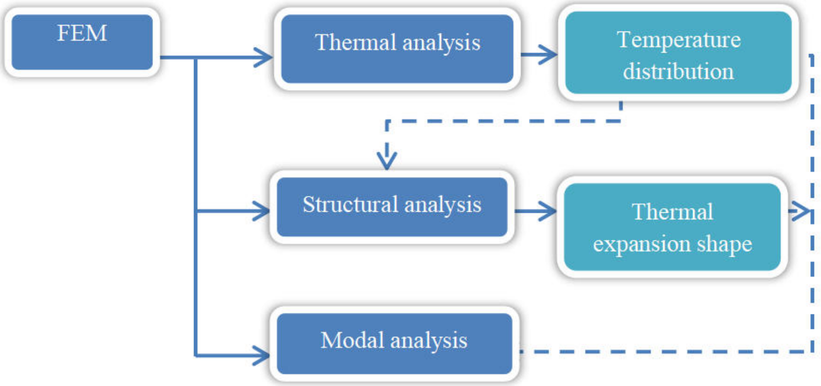

Figure 3. Analysis principles of an ultrasonic vibration device.

Modal analysis, a branch of structural dynamics, can analyze the vibration of a structure under no-load conditions, as well as structures with prestress. The analysis results reveal information such as resonant frequencies, vibration modes, and relative displacement distribution. Modal analysis is a type of linear analysis that mainly explores the natural frequencies and vibration modes of a structure. Regardless of whether there is damping, it will eventually be reduced to a problem of standard eigenvalues and eigenvectors.

Frequency Response Analysis (or harmonic response) is the steady-state response of a structure under a sinusoidal load applied at different frequencies. This allows for the analysis and calculation of the relationship between the response value and frequency. The peak response can be found from this relationship curve, and the displacement, stress, etc., corresponding to this frequency can be further observed.

2.2. Experiments

As shown in **Figure 4**, the ultrasonic vibration device used in this study was provided by King Ultrasonic Co., Ltd. The output frequency of the frequency generator was within an automatic tuning range of 35.1 kHz to 35.5 kHz. The transducer contained four stacked PZT-8 piezoelectric ceramic plates, and the horn was designed as a stepped cylinder. This horn design is to enlarge the forming area of the molding machine based on considering machine limitations and manufacturing factors (**Figure 5**).

To generate a controlled temperature gradient within the ultrasonic device, a specialized thermal management system consisting of a water cooler and an infrared heater was integrated into the horn assembly. As shown in **Figure 6**, the cooling unit was positioned at the upper section of the horn to protect the transducer, while the infrared heater was located at the base. A Yokogawa (UP150) temperature controller regulated the heater's power output based on feedback from a thermocouple positioned 5 mm from the horn's bottom tip. Thermal profiles were monitored via additional thermocouples at 15 mm, 30 mm, 50 mm, and 90 mm intervals from the bottom. To characterize the system's dynamic behavior under these thermal conditions, an

HP (8751A) network analyzer was utilized to record the frequency response and determine damping ratios. Furthermore, a Keyence (H020) laser displacement sensor was employed to quantify both the thermal expansion and the vibration amplitude during transducer activation.

(a) **(b)** **(c)**

Figure 4. Ultrasonic vibration device: **(a) Ultrasonic** generator; **(b)** Transducer & booster; **(c)** Horn.

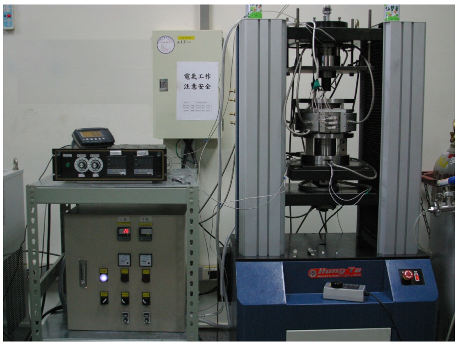

Figure 5. Glass molding machine.

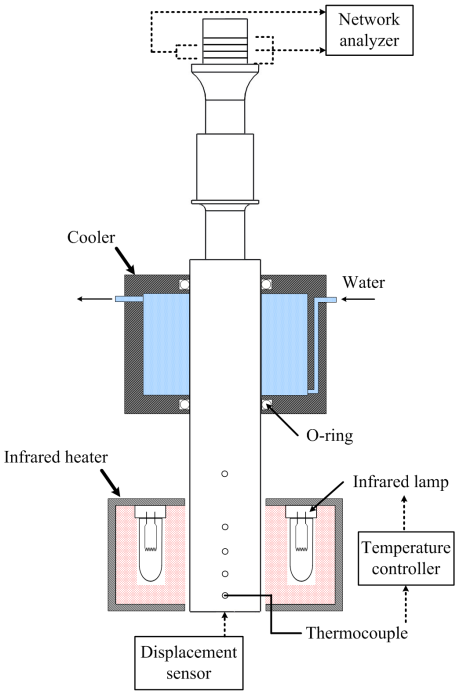

Figure 6. Schematic diagram of the heating experiment.

2.3. Thermal-structural modal analysis workflow

Numerical simulations were performed using the ANSYS finite element software package. As illustrated in the multi-physics workflow, the process began with a steady-state thermal analysis to establish the temperature profile across the ultrasonic assembly. These thermal results were then imported into a structural analysis to account for thermal expansion effects. Subsequently, the updated geometry and material properties were utilized in modal and harmonic response analyses to identify the vibration modes, resonant frequencies, and displacement amplitudes of the heated device. To streamline the computational model, the threaded connections between the transducer, booster, and horn were represented as solid volumes with continuous interfaces, and the thickness of the electrode plates within the piezoelectric stack was omitted from the simulation.

2.3.1. Material properties

Tables 1 and **2** list the mechanical and thermal properties of components in the ultrasonic vibration device. The input material properties of the piezoelectric ceramics were [25]:

Elastic constants:

$$\left[K^{E}\right]=\begin{bmatrix}137 & 69.7 & 0 & 0 & 0\\ 69.7 & 137 & 0 & 0 & 0\\ 71.6 & 71.6 & 0 & 0 & 0\\ 0 & 0 & 33.65 & 0 & 0\\ 0 & 0 & 0 & 31.4 & 0\\ 0 & 0 & 0 & 0 & 31.4\end{bmatrix}\text{GPa} \tag{3}$$

Piezoelectric stress constants:

$$[e]=\begin{bmatrix}0 & 0 & 0 & 0 & 0 & 10.4\\ 0 & 0 & 0 & 0 & 10.4 & 0\\ -4 & -4 & 13.8 & 0 & 0 & 0\end{bmatrix}\mathrm{C/m^2} \tag{4}$$

Dielectric relative permittivity matrix:

$$\left[e^{S}\right]=\begin{bmatrix}898 & 0 & 0\\ 0 & 898 & 0\\ 0 & 0 & 582\end{bmatrix}. \tag{5}$$

Table 1. Mechanical properties for components in the ultrasonic vibration device.

	Density (kg/m^3)	Young's modulus (GPa)	Poisson's ratio
Transducer (A2024)	2,780	69	0.33
Piezoelectric (PZT-8)	7,600	–	0.29
Booster (Ti64)	4,430	113.8	0.342
Horn (SUS304)	7,900	Elevated temperature physical properties of stainless steels [26]	0.3

Table 2. Thermal properties for components in the ultrasonic vibration device.

	Thermal conductivity (W/m.°C)		Coefficient of thermal expansion (10×10^{-6}/°C)		Specific heat (J/kg. °C)	
Transducer	237		23		897	
Piezoelectric	20		2.6		-	
Booster	22		8.6		523	
Horn	200 °C	15	100 °C	16.3	25 °C	456
	400 °C	17.5	200 °C	17.8	90 °C	490
			300 °C	17.2	200 °C	532
			400 °C	17.8	320 °C	557
			500 °C	17.2	430 °C	574
					540 °C	586

The dielectric constant in a vacuum was 8.85×10^{-15} F/m. Since the thermal gradient was primarily concentrated within the horn, temperature-dependent material properties were specifically assigned to this component. For computational efficiency, the thermal simulation focused on conductive heat transfer, omitting the effects of convection and radiation.

Since this study focuses on a vibration system using a piezoelectric transducer and considers temperature factors, elements suitable for coupled fields are used to perform coupling analysis of different physical fields. The ultrasonic vibration device in this study is a complex three-dimensional model. Generating a hexahedral mesh requires careful mesh planning. Second-order tetrahedral elements are employed to mitigate shear locking and improve displacement accuracy of first-order tetrahedral meshes. Therefore, second-order tetrahedral meshes are chosen for this study, as they easily generate meshes even for complex geometries, and ANSYS has an automatic mesh generation function.

Considering the need for piezoelectric coupling analysis (structure-electricity) of the piezoelectric effect in the oscillator and heat transfer analysis (thermal-structure) of the amplifier under different temperature distributions, this study selected SOLID98, a three-dimensional second-order tetrahedral mesh system, as the mesh system for this model. SOLID98 in ANSYS is a ten-node tetrahedral mesh, with each node having six degrees of freedom (UX, UY, UZ, TEMP, VOLT, MAG), suitable for three-dimensional coupled analysis of electromagnetic, thermal, electric, piezoelectric, and structural fields.

2.3.2. Boundary conditions

In the experiment, the fixed end of the vibration system was achieved by clamping the upper and lower edges of the flange of the transducer using a fixture. Therefore, setting the upper and lower surfaces of the flange to have no vertical displacement is closer to reality than setting it to be completely fixed. The polarization direction of the piezoelectric sheet is the Z-axis for odd-numbered layers and the opposite for even-numbered layers. Since the polarization direction of the piezoelectric material matrix is the Z-axis, the coordinate matrix of the second and fourth piezoelectric sheets is set to be opposite to that of the other two sheets (i.e., -Z- axis) using region coordinates. In addition, since the electrode plate was ignored and replaced by a surface when building the model, the first, third, and fifth surfaces were set to ground (voltage is zero) in the same way as the electrode plate. The voltage values measured in the experiment were input to the second and fourth surfaces, as shown in **Figure 7**. **Table 3** shows the temperature distribution of the horn, which signals received from thermal couples. The distance step size shifts from uniform 5 mm increments to a single 105 mm interval because the region spanning from 20 mm to 105 mm tracks the acoustic node of the acoustic horn structure. Within this stable region, the geometric sensitivity to localized thermal fluctuations is minimal, allowing for a consolidated long-interval parameter assignment without sacrificing calculation accuracy. The peripheral outer surface boundary of the upper assembly was set to a constant 25 °C to simulate active liquid cooling. For model connectivity, individual elements were coupled at solid boundaries as a single unified piece with heterogeneous material domain assignments. **Figure 7** illustrates the applied transducer boundary configurations. Furthermore, in the structure of the vibration system, each part is connected by screws, but in this finite element model, all objects are treated as a single piece, and parameters are given for different materials before simulation.

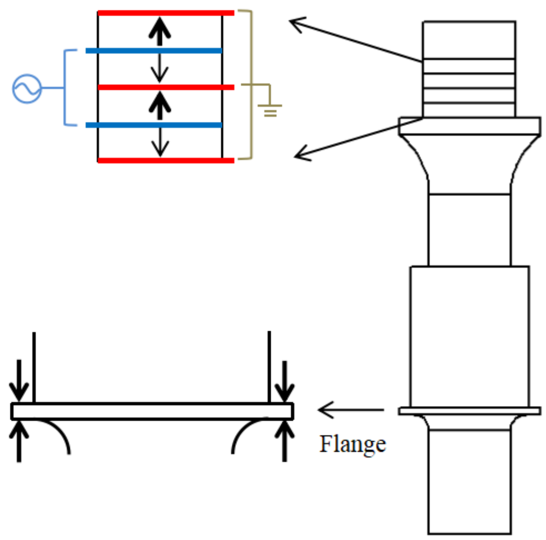

Figure 7. Boundary conditions on the transducer and booster.

Table 3. Temperature distribution of the horn.

Distance from horn end (mm)	Temperature (°C)
5	500
10	493
15	485
20	475
105	25

2.4. Optimization process

This study utilizes SmartDO as a numerical optimization platform that automates FEA/CAD workflows by using intelligent algorithms to control design variables. The integration with ANSYS is established by modifying the Jobname.log process file, which records the simulation steps. The optimization setup requires three Tcl script files to define the objective function, design constraints, and variable initialization.

These files are executed in a unified directory to perform cascaded finite element and optimization analyses. Upon convergence, the results are verified within ANSYS to ensure the accuracy of the optimized design. **Figure 8** indicates the optimization procedure.

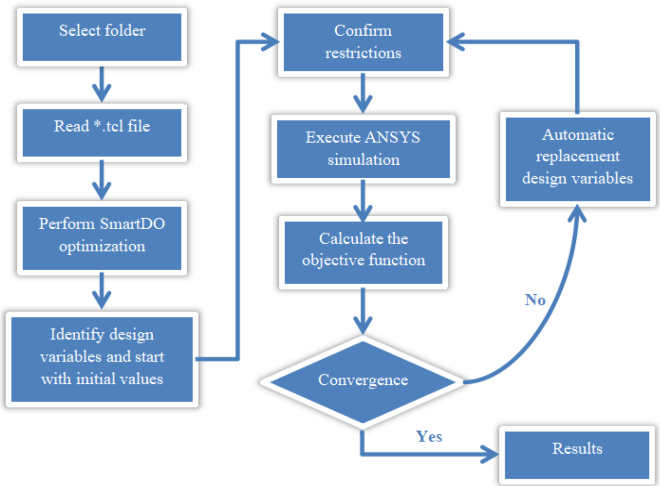

Figure 8. Automated optimization procedure.

To maximize output uniformity across the tool face under severe non-linear high-temperature gradients, the normalized objective uniformity variance variable, Φ, must be minimized:

$$\Phi = \frac{|U_{max} - U_{min}|}{|U_{max}|} \tag{6}$$

where U_{max} and U_{min} represent the maximum and minimum longitudinal displacement amplitudes calculated across the extreme output end face of the horn, respectively. Design variables are shown in **Figure 9** and listed in **Table 4**.

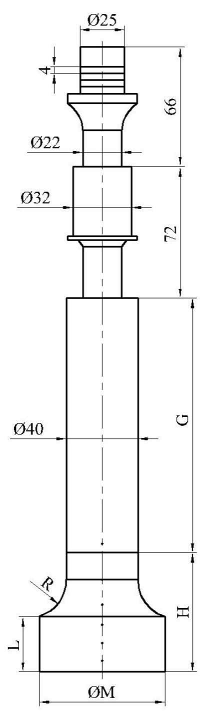

Figure 9. Design variables on the horn.

Table 4. Setting for design variables with different horn end diameters.

	Range	Initial value
M	-	60 mm, 65 mm, 70 mm, 75 mm, 80 mm, 85 mm, 90 mm
H	40 mm ~ 80 mm	65 mm
L	20 mm ~ 60 mm	30 mm
R	5 mm ~ 9 mm	8.5 mm
G	130 mm ~ 150 mm	140 mm

The system optimization process was governed by the following geometric and frequency constraints:

$$\begin{cases} \lvert \text{frequency} - 35,300 \text{ Hz} \rvert \leq 200 \text{ Hz} \\ \hline \lvert \text{G} + \text{H} - 237 \rvert \leq 35 \text{ mm} \end{cases} \tag{7}$$

3. Results and discussion

3.1. Optimization of horn shape

The optimization results and corresponding performance metrics are summarized and illustrated in the following tables and figures. **Table 5** presents the optimization outcomes for various horn end diameters, while the convergence behavior of the objective function is plotted in **Figure 10**. The data indicate that while amplitude uniformity tends to decrease as the end diameter increases, the degradation remains marginal for diameters within the 60 mm range. In the case of a 60 mm horn end diameter, the final geometry of the optimized vibration device is depicted in **Figure 11**. Also, the modal characteristics and the longitudinal relative displacement distribution at the resonant frequency are presented in **Figure 12**, with the specific displacement profile across the horn's output end face shown in **Figure 13**.

Table 5. Results of preliminary optimized design for different horn end diameters.

ΦM (mm)	H (mm)	L (mm)	R (mm)	G (mm)	Resonant frequency (Hz)	Amplitude damping ratio (%)
60	64.000	31.973	8.550	140.000	35,365	8.75
65	66.420	37.200	10.657	139.952	35,182	8.47
70	67.391	41.241	13.798	140.032	35,117	7.52
75	120.000	75.000	16.500	141.811	35,161	46.53
80	119.965	56.030	16.957	145.318	35,382	12.89
85	115.090	64.818	16.647	141.967	35,100	48.49
90	110.597	59.165	18.157	142.471	35,106	50.52

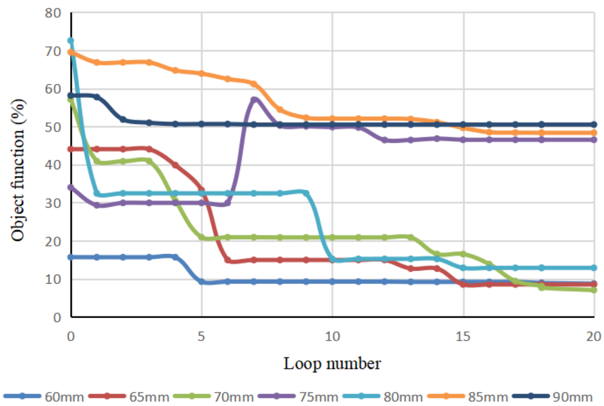

Figure 10. Convergence behavior of the objective function.

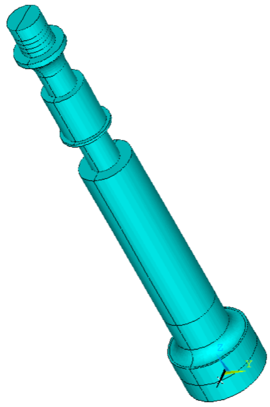

Figure 11. Final geometry of the optimized horn in the case of a 60 mm horn end diameter.

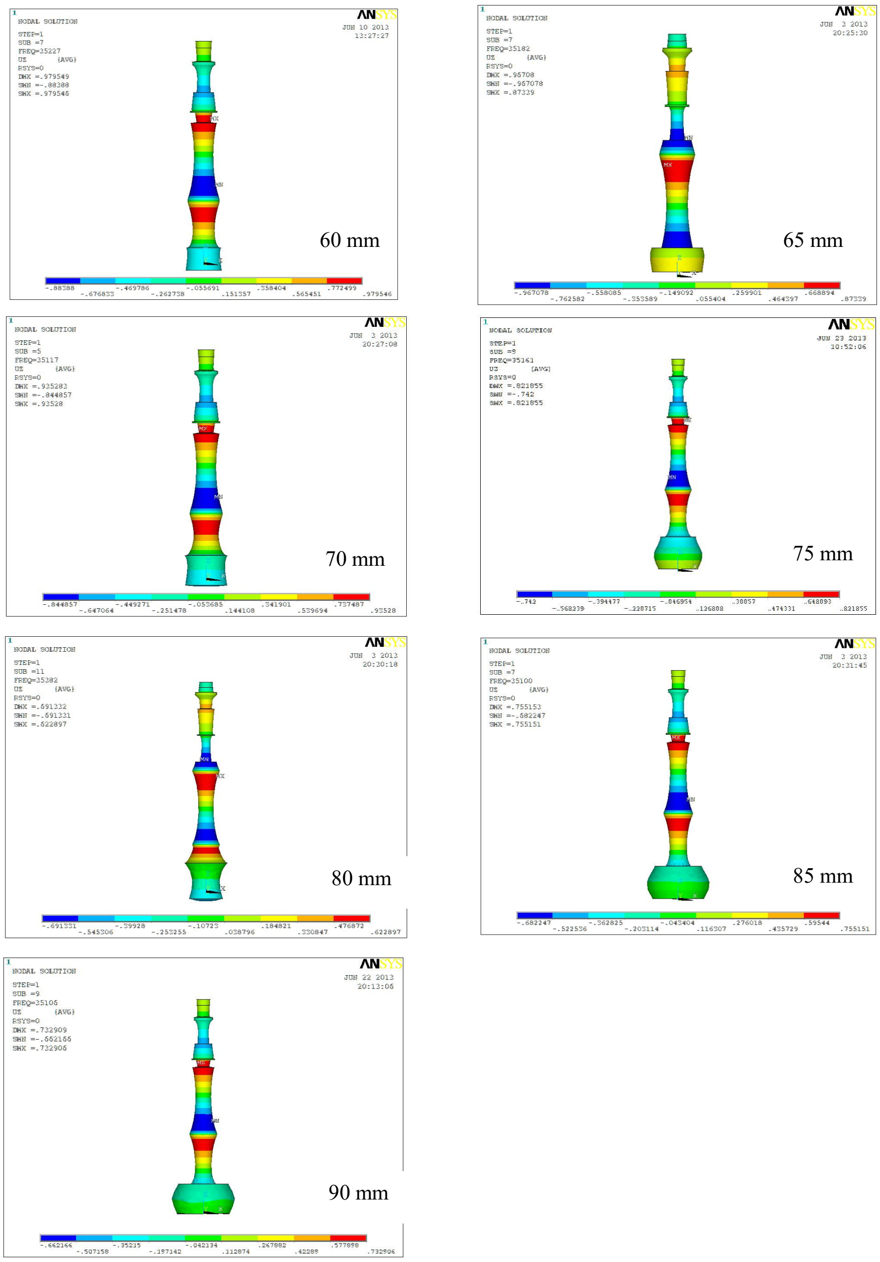

Figure 12. Longitudinal relative displacement distribution of the optimized horn at the resonant frequency in case of different horn end diameters.

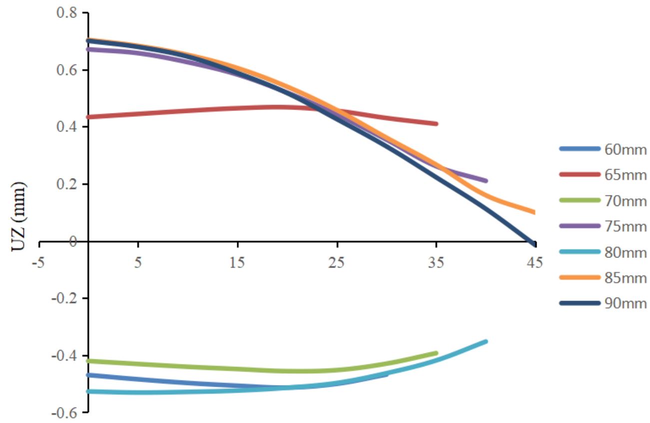

Figure 13. Displacement profile across the horn's end face with different horn end diameters.

Table 5 shows that the amplitude uniformity is 7.52% when the horn end diameter is 70 mm, and the output surface diameter affects the amplitude uniformity. To obtain an amplitude uniformity higher than 7.52%, the output surface diameter (M) is added to the design variables. The modified **s**ettings for design variables are shown in **Table 6**. The results of final optimization are shown in **Table 7** and **Figures 14–16**.

Table 6. Modified settings for design variables.

	Range	Initial value
M	60 mm ~ 90 mm	69 mm
H	40 mm ~ 80 mm	70 mm
L	20 mm ~ 70 mm	35 mm
R	5 mm ~ 12.5 mm	10.5 mm
G	130 mm ~ 150 mm	140 mm

Table 7. Results of final optimization for different horn end diameters.

	ΦM (mm)	H (mm)	L (mm)	R (mm)	G (mm)	Resonant frequency (Hz)	Amplitude damping ratio (%)
Initial values	69.000	70.000	35.000	10.500	140.000	34141	57.85
Optimized values	68.642	67.616	41.584	10.628	139.498	35141	6.76

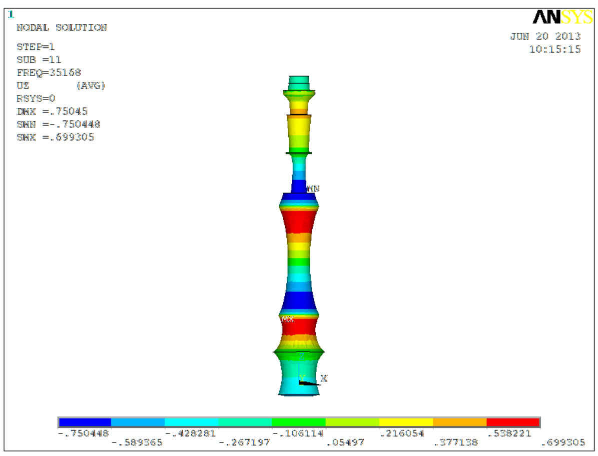

Figure 14. Displacement distribution of the optimized ultrasonic device after final optimization.

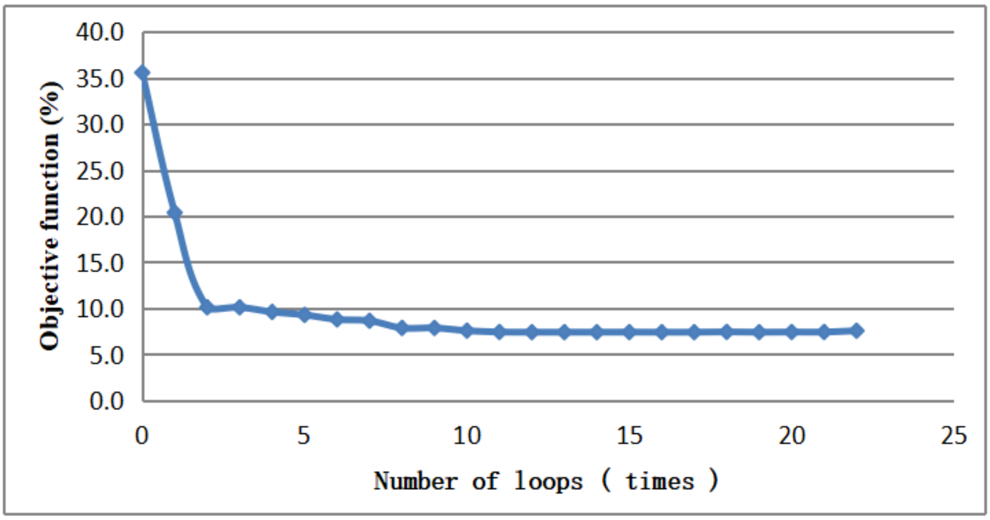

Figure 15. Convergence behavior of the objective function after final optimization.

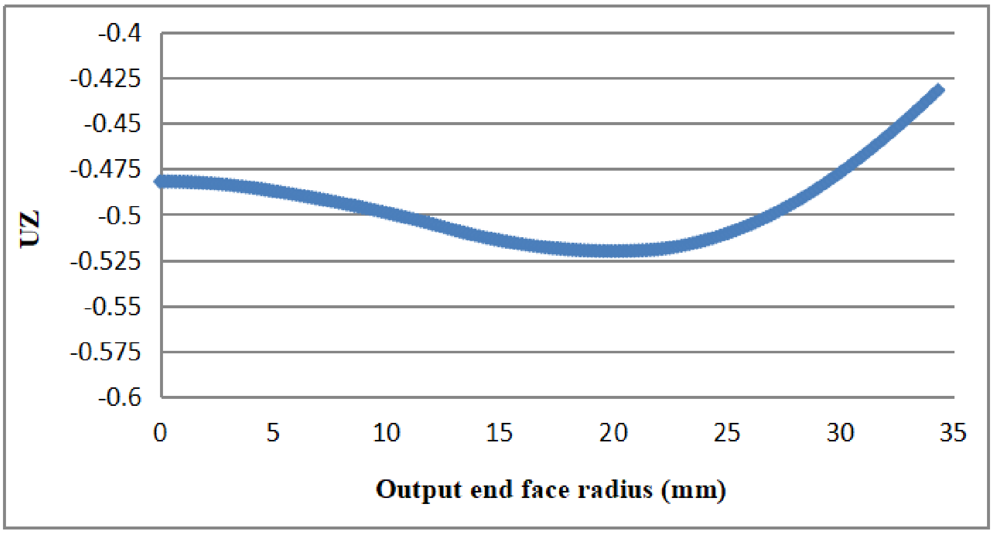

Figure 16. Displacement profile across the horn's end face after final optimization.

3.2. Experimental validation

Experimental measurements were conducted on the final optimized shape of the horn at an operating temperature of 500 ℃, including resonant frequency and vibration amplitude (**Figures 17** and **18**). As shown in **Figure 19**, the resonant frequency from the signal of the network analyzer is 35,068 Hz, while that searched by the electronic signal generator is 35,030 Hz, which is very close to the resonant frequency obtained by the network analyzer. When the system vibrates, the amplitude at the bottom of the horn is measured using a laser sensor. Since the electronic signal generator inputs a high-frequency sinusoidal voltage to the piezoelectric element, the amplitude at the bottom of the horn is also a sinusoidal mechanical vibration. Vibration amplitude measurements show that the maximum amplitude is 4.71 μm, and the minimum amplitude is 4.33 μm. Therefore, the amplitude uniformity is approximately 6.76% (**Figure 20**).

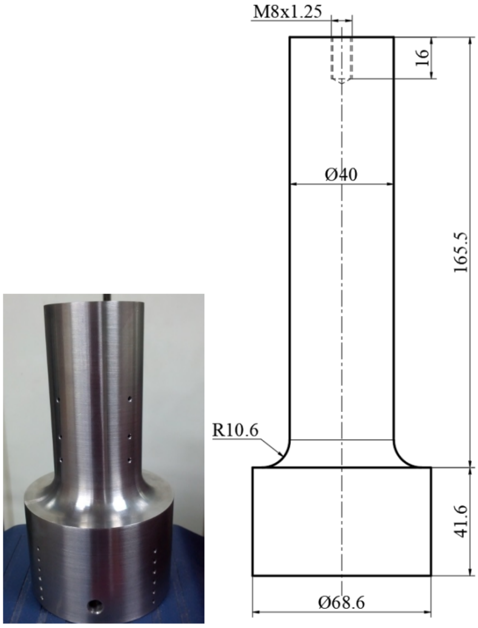

Figure 17. Optimized horn design.

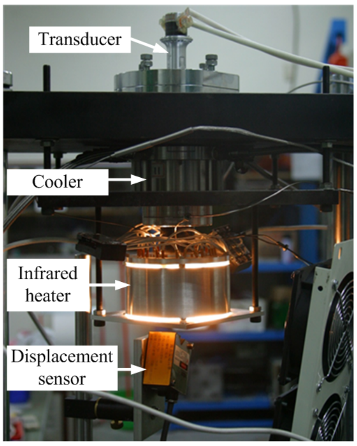

Figure 18. Setup of an ultrasonic vibration system at elevated temperature.

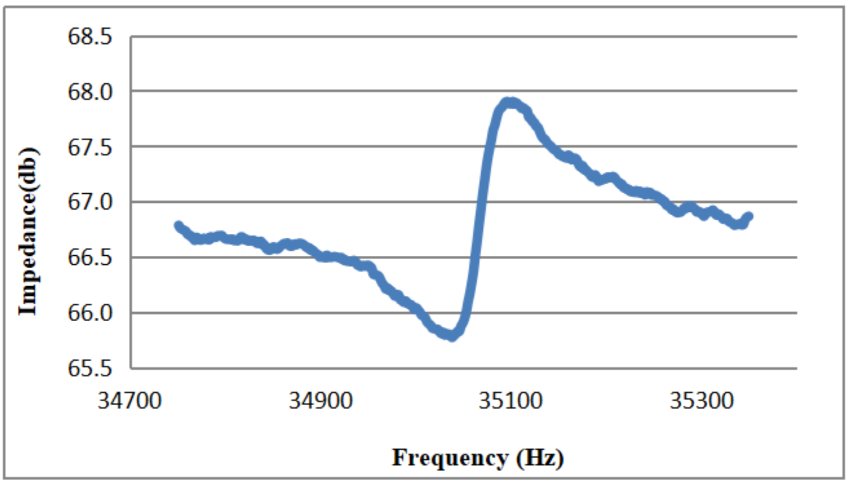

Figure 19. Signal values of the network analyzer at high temperature.

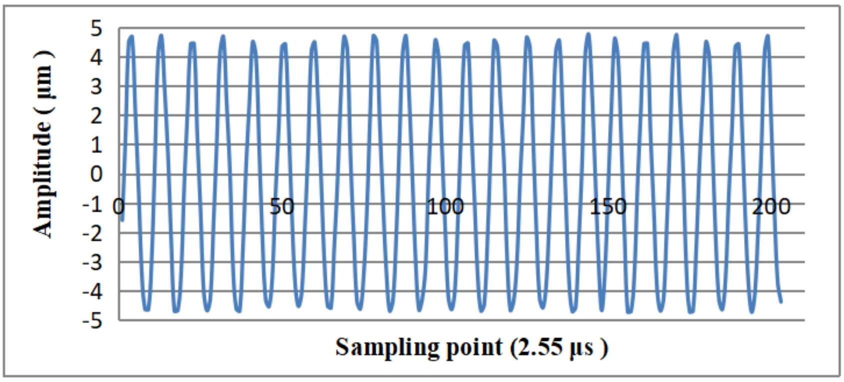

Figure 20. Vibration amplitude measurement.

Because raw displacement values extracted via FEA calculations correspond to normalized modal eigenvectors, the maximum values from both the numerical simulation and empirical test data were scaled to unity to ensure a valid comparison. The normalized amplitude distribution comparison along the output face radius is displayed in **Figure 21**. The comparison reveals that the spatial displacement trends calculated via the multi-physics optimization model match the physical experimental profiles. The marginal discrepancy between the simulated variation index (6.76%) and the physical laboratory test configuration (8.20%) is attributed to three primary physical phenomena:

- Mathematical discretization and energy losses: Minor mesh topology deviations and the omission of convective and radiative thermal dissipation loops in the FEA code;
- Material property heterogeneity: Variances between the pristine isotropic material curves specified in software databases and the actual commercial SUS304 parent stock;
- Fabrication tolerances: Minor millimeter-level geometric errors introduced during CNC machining of the transition paths, along with slight contact pressure variances across the threaded coupling bolts.

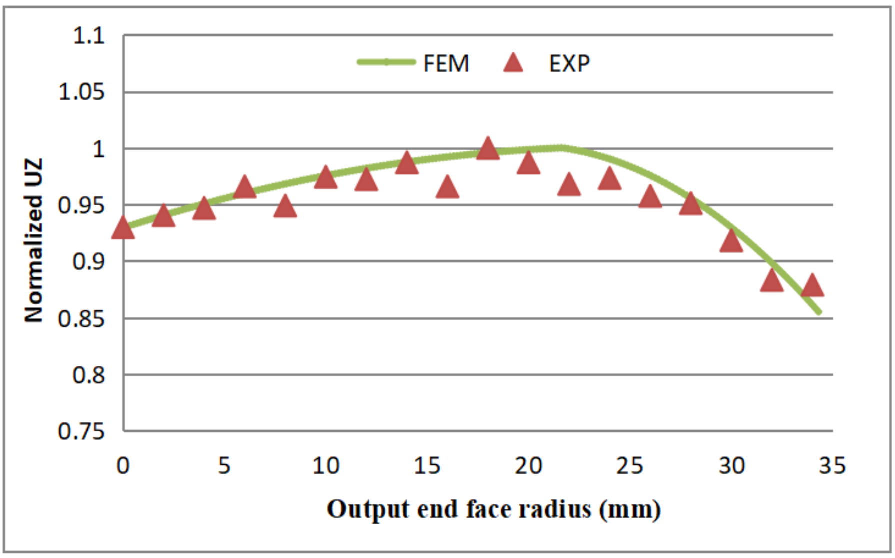

Figure 21. Comparison of output end-face amplitude distribution between room temperature experiment and simulation.

4. Conclusion

This study has successfully demonstrated a multi-physics shape optimization methodology for high-power ultrasonic resonators operating under severe non-linear temperature gradients up to 500 °C. The central conclusions derived from this research are itemized as follows:

- Thermal-acoustic coupling validation: A strong correlation was established between temperature-dependent reductions in material Young's modulus and physical acoustic frequency drift, validating the accuracy of the multi-physics FEA model.
- Automated geometric resolution: The automated optimization interface connecting ANSYS with SmartDO successfully balanced conflicting constraints, engineering a horn geometry that restricted structural non-uniformity to 6.76% while maintaining target resonance.
- Industrial feasibility: High-temperature laboratory testing confirmed that the optimized stack limits thermal drift to a narrow window (84–99 Hz), allowing standard industrial generators to maintain lock without triggering overload conditions.

While the developed shape optimization routine demonstrates excellent experimental performance, certain limiting factors remain that present opportunities for future research:

- Isotropic boundary approximations: The computational framework assumed isotropic material behavior and omitted micro-scale interfacial damping across the structural joints. Future studies will incorporate advanced three-dimensional fractal models of thermal contact conductance to capture real-world micro-contact mechanics at the booster-horn interface.
- Transient thermal fatigue analysis: Physical testing was conducted under steady-state thermal profiles. Future research will focus on investigating long-term creep behavior, thermal fatigue under rapid cyclic temperature transitions, and structural damping variations during continuous processing.

Author contributions: Conceptualization, LN; methodology, CH; software, LN; validation, LN; formal analysis, CH; investigation, LN; resources, CH; data curation, LN; writing—original draft preparation, LN; writing—review and editing, CH; visualization, LN; supervision, CH; project administration, LN; funding acquisition, LN. All authors have read and agreed to the published version of the manuscript.

Funding: This research was funded by Hanoi University of Science and Technology, grant number T2024-PC-035.

Institutional review board statement: Not applicable.

Informed consent statement: Not applicable.

Data availability statement: The data supporting the findings of this study are included within the article. Additional data are available from the corresponding author upon reasonable request.

Acknowledgment: The authors would like to thank Dr. Chen Shen-Yeh for supporting SmartDO software. Many thanks are also sent to members of the Precision Engineering & Simulation Laboratory at the Department of Mechanical Engineering, National Yang Ming Chiao Tung University, Taiwan for their experimental setups.

Conflict of interest: The authors declare no conflict of interest.

AI use statement: During the preparation of this manuscript, the authors used Gemini solely for language refinement and structural formatting based on reviewer feedback. No AI tools were used for data analysis, interpretation, or generation of scientific content. All outputs were critically reviewed and edited by the authors. The authors take full responsibility for the integrity and accuracy of the work.

References

1. Li H, Chen T, Bie W, et al. Multi-Step Two-Dimensional Ultrasonic-Assisted Grinding of Silicon Carbide: An Experimental Study on Surface Topography and Roughness. Micromachines. 2024; 15(7): 915. doi: 10.3390/mi15070915
2. Jin J, Mao J, Wang R, et al. Experimental Study on Ultrasonic Vibration-Assisted Grinding of SiCp/Al Composites Grinding. Micromachines. 2025; 16(3): 302. doi: 10.3390/mi16030302
3. Liu C, Zhang Y, Zhu L, et al. A Review of Ultrasonic Vibration-Assisted Grinding for Advanced Materials. Intelligent and Sustainable Manufacturing. 2025; 2(1): 10001. doi: 10.70322/ism.2025.10001
4. Yin P, Li W, Xu C, et al. Influence of Single-Sided Ultrasonic Assistance on the Double-Sided Welding Forming Quality of Q355 Thin Plates. Metals. 2026; 16(1): 58. doi: 10.3390/met16010058
5. Liang H, Shi X, Li Y. Effect of Ultrasonic Assistance on Properties of Ultra-High-Strength Steel in Laser-Arc Hybrid Welding. Coatings. 2025; 15(4): 389. doi: 10.3390/coatings15040389
6. Ma C, Liu Y, Li H, et al. Ultrasonic assisted additive manufacturing of Al–Mg alloys: Microstructure refinement and mechanical improvement through meltable ultrasonic probe. Journal of Materials Processing Technology. 2026; 351: 119278. doi: 10.1016/j.jmatprotec.2026.119278
7. Liu S, Dung Y. Hot embossing precise structure onto plastic plates by ultrasonic vibration. Polymer Engineering & Science. 2005; 45(7): 915–925. doi: 10.1002/pen.20357
8. Hung JC, Hung C. The influence of ultrasonic-vibration on hot upsetting of aluminum alloy. Ultrasonics. 2005; 43(8): 692–698. doi: 10.1016/j.ultras.2005.03.001
9. Nguyen L. Elimination of air entrapment in microstructures glass embossing process using ultrasonic vibration. Solid State Technology. 2020; 63(6): 4539–4548. Available online: https://solidstatetechnology.us/index.php/JSST/article/view/3841
10. Yu SW, Du N, Gu B, et al. Thermal Effects on Fracture of Piezoelectric Materials. Journal of Intelligent Material Systems and Structures. 2005; 16(7–8): 567–572. doi: 10.1177/1045389X05051074
11. Baptista F, Budoya D, Almeida V, et al. An Experimental Study on the Effect of Temperature on Piezoelectric Sensors for Impedance-Based Structural Health Monitoring. Sensors. 2014; 14(1): 1208–1227. doi: 10.3390/s140101208
12. Sun X, Xing W. Fractal model of thermal contact conductance of rough surfaces based on elliptical asperity. Industrial Lubrication and Tribology. 2023; 75(4): 424–431. doi: 10.1108/ILT-02-2023-0035
13. Zhao Y, Fang C, Cai L, et al. A three-dimensional fractal theory based on thermal contact conductance model of rough surfaces. Proceedings of the Institution of Mechanical Engineers, Part E: Journal of Process Mechanical Engineering. 2018; 232(5): 528–539. doi: 10.1177/0954408917727198
14. Sun X. Fractal model of thermal contact conductance of rough surfaces considering substrate deformation. Industrial Lubrication and Tribology. 2023; 75(8): 895–903. doi: 10.1108/ILT-03-2023-0074
15. Afshari M, Arezoo B. Design of wide ultrasonic horns based on topology optimization. Engineering Optimization. 2022; 54(6): 907–927. doi: 10.1080/0305215X.2021.1901285
16. Schmidt S, Wadbro E, Berggren M. Large-Scale Three-Dimensional Acoustic Horn Optimization. SIAM Journal on

Scientific Computing. 2016; 38(6): B917–B940. doi: 10.1137/15M1021131
17. Dong H, Shen Y, Gao H. Shape optimization of acoustic horns using the multimodal method. The Journal of the Acoustical Society of America. 2020; 147(4): EL326–EL332. doi: 10.1121/10.0001037
18. Dong H, Doc JB, Félix S. Efficient multimodal-based shape optimization of acoustic horns with application to subwavelength perfect transmission. Journal of Sound and Vibration. 2023; 559: 117746. doi: 10.1016/j.jsv.2023.117746
19. Mubashir M, Mutahir R, Ur Rehman MS. Design and Analysis of Hollow Catenoidal Horn Profile for Ultrasonic Machining of Composite Materials. Journal of Studies in Science and Engineering. 2022; 2(2): 18–32. doi: 10.53898/josse2022222
20. Addamo G, Scalcinati L, Zannoni M, et al. Feasibility Study on Additive Manufacturing of Feed Horn Operating in D-Band. Sensors. 2025; 25(2): 523. doi: 10.3390/s25020523
21. Wada Y, Nakamura K. Topology optimization of large ultrasonic tools for uniform vibration using level-set method. Japanese Journal of Applied Physics. 2025; 64(3): 03SP34. doi: 10.35848/1347-4065/adb296
22. Your Piezo Experts. Available online: http://www.piezo.com (accessed on 12 January 2026).
23. BEK Ultrasonic. Available online: http://www.bekultrasonics.com (accessed on 12 January 2026).
24. Zhendong Z. Ultrasonic Engineering, 1st ed. Quanhua Science and Technology Book Co., Ltd.; 1999.
25. Amin SG, Ahmed MHM, Youssef HA. Computer-aided design of acoustic horns for ultrasonic machining using finite-element analysis. Journal of Materials Processing Technology. 1995; 55(3–4): 254–260. doi: 10.1016/0924-0136(95)02015-2
26. Elevated temperature physical properties of stainless steels. Available online: https://bssa.org.uk/bssa_articles/elevated-temperature-physical-properties-of-stainless-steels/ (accessed on 12 January 2026).